Available online at www.sciencedirect.com

SCIENCE DIRECT®

ELSEVIER

Coastal Engineering 52 (2005) 887–913

Coastal Engineering
An International Journal for Coastal, Harbour and Offshore Engineers

www.elsevier.com/locate/coastaleng

Modelling of velocity and turbulence fields around and within low-crested rubble-mound breakwaters

Inigo J. Losada [a,*], Javier L. Lara [a], Erik D. Christensen [b], Nicolas Garcia [a]

[a] *Ocean and Coastal Research Group, University of Cantabria, Dpto. de Ciencias y Técnicas del Agua y del Medio Ambiente, E.T.S.I. de Caminos, Canales y Puertos. Avda. de los Castros s/n, Santander, 39005, Spain*
[b] *DHI Water and Environment, Denmark*

Abstract

A description of the progress achieved within DELOS (environmental DEsign of LOw-crested coastal defence Structures) EU project in the modelling of wave interaction with low-crested structures (LCS) is presented in this paper. Emphasis is put on the description of the near-field flow, especially the velocity and turbulence distribution around and inside LCS, as required by other researchers in the project. Two-dimensional (VARANS) and three-dimensional (LES) numerical modelling has been considered. The two-dimensional model has been extensively validated with DELOS laboratory data as shown in Garcia et al. [Garcia, N., Lara, J.L., Losada, I.J., 2004. 2-D Numerical analysis of near-field flow at low-crested breakwaters. Coastal Engineering, ELSEVIER, 51 (10) 991–1020]. A system of flow recirculation is included in both the experimental and numerical set-ups for a correct description of the 2DV velocity field in the vicinity of the structure. Further validation is presented in this paper. Laboratory tests on two values of crest width have been simulated in order to analyse relevant near-field flow features related to a variation of the geometric configuration of the structure. The width of the breakwater crest is seen to significantly influence the wave breaking-induced flow pattern at the structure. Magnitudes such as turbulent kinetic energy (TKE), TKE dissipation rate, shear stresses and Reynolds stresses are computed around and inside the breakwater. The three-dimensional model numerical results are compared with results of wave basin experiments, showing a good agreement for instantaneous free surface. Numerical results of the flow over the breakwater and around the breakwater head are also presented.

1. Introduction

The objective of this paper is to make a description of the state of the art and progress within DELOS in the modelling of wave interaction with low-crested structures (LCS). Most of our efforts within DELOS have been focused on the 2-D and 3-D numerical modelling of LCS functionality. Therefore, most of the paper will be devoted to the description of the models and their exploitation.

Four main reasons account for the analysis of the flow and associated velocities around and within low crested structures: structure functionality, structure stability, implications on the morphodynamics of nearby areas and the analysis on the distribution

---

* Corresponding author.
E-mail address: losadai@unican.es (I.J. Losada).

0378-3839/$ - see front matter © 2005 Elsevier B.V. All rights reserved.
doi:10.1016/j.coastaleng.2005.09.008

and mortality of organisms attached or living in the LCS.

Design conditions for LCS should include a correct assessment of the functionality of the structure. The most relevant hydraulic processes to be considered at wave and LCS interaction encompass primarily wave reflection, wave dissipation and wave transmission resulting from wave overtopping and wave penetration through the porous structure. Especially, there is a lack of knowledge in the interpretation and modelling of the generation of higher harmonics and its influence on wave transmission. The modelling of the dissipation mechanisms due to wave breaking, turbulence and generation of eddies in the fluid region as well as turbulence and friction within the porous material is also not well established.

The stability of LCS armour layers has been studied for several years, and formulations for damage assessment can be found in the literature. Most of these formulations are based on laboratory tests for both regular and irregular waves. In general, the stability of a submerged structure has been related to a Shield's type parameter, known as the mobility parameter (Vidal et al., 1998), which compares the drag forces with the stone weight or other approximations based on the evaluation of the Morison forces on the stones. Both the mobility parameter approach and the formulation of the Morison forces require the evaluation of the velocity profile over the structure, which is generally unknown. So far, this velocity is computed using linear wave theory or other nonlinear wave theories. However, most of the calculated velocities seem to deviate from experimental measurements, due to various reasons. Moreover, the wave-induced flow within the porous media will also affect stone stability, since the pore pressure and the seepage velocity may reduce the effective stone weight. In general, the effects of the porous flow on the fluid velocities are not considered.

The breaking process over the overtopped structure enhances the pumping of wave-induced mass fluxes over the low-crested detached structure. This results in an enhanced near shore circulation and consequently the presence of the LCS modifies the sediment fluxes and morphodynamics evolution. Furthermore, the fluxes through the permeable structure may also contribute to additional modifications. Consequently, circulation and morphodynamic models assessing morphodynamic evolution in the presence of LCS should include additional information regarding the fluxes on the top and through the structure. This is only possible based on an appropriate modelling of the velocity field and breaking processes in the near field of the structure and how those are affected by incident wave parameters, structure geometry and permeable material characteristics.

It is well established that hydrodynamic forces due to breaking waves are among the most important sources of shore organism distribution and mortality. Therefore, in order to interpret the biomechanical characteristics of the epibiota on a low-crested structure, to evaluate stress levels resulting in tissue damages or complete dislodgement, to establish the average flow conditions to predict larval settlement and delivery of nutrients or the critical periods of very low flow speed causing hypoxia, a feasible description of the flow is required.

In the literature, the analysis of wave interaction with LCS has been addressed based on physical and mathematical modelling. Most of the physical modelling has been oriented towards the functional design of LCS to evaluate reflection and transmission or to find empirical formulations for stability. Unfortunately, only a very limited number of laboratory experiments include velocity measurements around the structure. Most of the velocity measurements correspond to non-realistic structures such as submerged steps or impermeable structures or lack of enough spatial resolution or acquisition frequency to evaluate velocity gradients, flow inside the structure or turbulence. With regard to experimental work in the field, the lack of information on the functionality of LCS is even more important. To our knowledge, only a few experiences include velocity information.

Alternative approaches to evaluate velocities and turbulence intensity around low crested structures are based on analytical and numerical modelling of wave and LCS interaction. For a review see Garcia et al. (2004) or Losada (2003). Summarising it can be said that most of the mathematical modelling to date has presented several limitations. Most of the models are based on potential flow theory, therefore neglecting turbulence, or are based on vertically integrated models, therefore limiting the breaking modelling or leading to inaccurate velocities around the LCS. Furthermore, most of the recent models based on potential nonlinear transient wave theories neglect flow inside porous layers, as a consequence neglecting one of the main processes controlling wave transmission and breaking.

In the last few years, a new generation of models based on the Navier–Stokes equations have become available for the coastal engineering community. However, even if this kind of modelling is relatively extended in other fields such as mechanical and aerospace engineering, it is in its initial stage in the coastal engineering field. This is probably due to the large domains of interest and the ample range of Reynolds numbers of the flows considered.

In the frame of DELOS most of the numerical work to analyse the near-field flow in LCS has been based on two different numerical models originating from the Navier–Stokes equations. A two-dimensional model based on the Volume-Averaged Reynolds Averaged Navier–Stokes (VARANS) equations named COBRAS and a three dimensional model based on a Large Eddy Simulation (LES) approach. Each of the models has several advantages and disadvantages, as will be shown further.

The paper is organised as follows. After the Introduction, the general features of the VARANS model are presented. The next section includes results of velocities and turbulence intensity around low-crested structures under breaking wave conditions. After a short discussion of the advantages and disadvantages of the VARANS model, the three-dimensional LES model is presented introducing some of its general features. Comparison of numerical results with experimental data follows. A specific study case related to a project study case is included in Appendix A. Finally, some conclusions are included.

2. 2DV modelling using VARANS equations

2.1. Description of the numerical model

The COBRAS model (Lin and Liu, 1998; Liu et al., 1999, 2000; Hsu et al., 2002) solves the 2DV Reynolds Averaged Navier–Stokes (RANS) equations, based on the decomposition of the instantaneous velocity and pressure fields into mean and turbulent components. Reynolds stresses are closed with an algebraic non-linear k–ε turbulence model that can solve anisotropic-eddy-viscosity turbulent flows. The flow in the porous structure is described in the COBRAS model by the Volume-Averaged Reynolds Averaged Navier–Stokes (VARANS) equations, obtained by integration of the RANS equations in a control volume larger than the pore structure but smaller than the characteristic length scale of the flow (see Hsu et al., 2002). A new set of k–ε equations equivalent to those of the fluid region are obtained by volume averaging and used to model turbulence production–dissipation within the porous media.

The movement of the free surface is tracked by the volume of fluid (VOF) method as described by Hirt and Nichols (1981) which satisfies both the kinematic and dynamic free surface boundary conditions for the mean flow and a non-slip boundary condition at the solid boundaries. With respect to the turbulence field, a log-law distribution of the mean tangential velocity in the turbulent boundary layer is considered near the solid boundary, where the values of k (turbulent kinetic energy) and ε (dissipation rate of turbulent kinetic energy) can be expressed as functions of the distance from the solid boundary and the mean tangential velocity outside the viscous sublayer. On the free surface, the zero gradient boundary conditions for both k and ε are based on the assumption of no turbulence exchange between the water and air. The initial condition consists of a still water situation, with no wave or current motion.

2.2. Presentation of the simulated laboratory tests

A complete description of the experiments carried out at the University of Cantabria for calibration, validation and application of the numerical results provided by the VARANS equations-based model can be found in Garcia et al. (2004) or in Kramer et al. (2005—this volume) included in the present issue.

In Garcia et al. (2004), the numerical simulation of a selection of tests on a wide-crested LCS (crest width: $b = 100$ cm) has been presented, with the aim of demonstrating the capability of the 2DV model to reproduce the main processes of wave interaction with LCS. The model was first calibrated on measured free surface data from one test on a submerged LCS, and then extensively validated on additional tests using experimental data of free surface displacement, bottom-pressure inside the breakwater core and horizontal and vertical particle velocities on the seaward slope of the structure.

The only parameters to be calibrated are the α and β porous media flow-friction coefficients of the VARANS equations (see Hsu et al., 2002, for equations and nomenclature). The obtained calibration values for these parameters ($\alpha=1000$ for both the armour layer and the core, and $\beta=0.8$ and 1.2 respectively) are within the state-of-the-art range of values (see e.g. Van Gent, 1994; Burcharth and Andersen, 1995; Liu et al., 1999). The porous media flow-friction coefficients were kept constant for the whole set of simulations, except for the case of the emerged non-overtopped LCS where overtopping is no longer the dominant process of transmission and consequently the flow conditions at the structure are very different compared with the other modelled cases of highly overtopped LCS ($\beta=0.4$ for the core, instead of 1.2 for negative or null freeboard structures). The stone nominal diameter and porosity defined as inputs for numerical modelling are the same as in the laboratory, i.e. 3.9 cm and 0.53 respectively for the armour layer, and 1.2 cm and 0.49 for the core.

In the following section, with the aim of providing additional results of the model validation and to assess the influence of the crest width on the near-field flow pattern, results of the simulation of wave interaction with a narrow-crest submerged breakwater ($b=25$ cm) are presented and compared with the results obtained with a wider crest of structure ($b=100$ cm). Comparisons of the numerical results with the available experimental data of velocity are presented. The numerical information, once validated, is then used to explore relevant aspects of the breaking wave-induced flow conditions at the structure that can hardly be examined based exclusively on the experimental approach.

2.3. Results of the numerical simulations

2.3.1. Wave field

The width of the breakwater crest is a key parameter in the functional design of a low-crested coastal defence structure as it determines to a large extent the structure performance in terms of energy dissipation and transmission. The same level of wave attenuation can be achieved with different combinations of structure freeboard and crest width. In particular, in coastal zones with strong aesthetics constraints a wide-crested slightly submerged structure can be preferred to a short-crested emerged structure with a similar rate of transmission. The crest width affects the mode of energy dissipation at the structure, and a combination of experimental and numerical results are used here to study the effect of a variation of the crest width on the wave breaking-induced near-field flow pattern.

In order to analyse the effect of the crest width on the velocity profiles, the velocity profiles, phase-averaged over 10 waves, at the front slope of the two different structure crest widths considered in the experimental setup are presented in Figs. 1 and 2, for each one of the three measured profiles and three sections at the crest region and the leeside slope. The target incident wave conditions are identical for both cases, wave height; $H=10$ cm, wave period; $T=1.6$ s and water depth: $h=40$ cm. Flow recirculation is included in both cases. Fig. 1 corresponds to the higher value of crest width while Fig. 2 shows the results for the narrow crest.

In both figures, the upper panel presents a partial view of the structure geometry including the location of the measurement profiles and velocity measurement points, as well as the considered sections at the crest and lee side. The wave height upper and lower envelopes together with the mean water level are also included, with dots corresponding to the experimental data and solid lines to the numerical results. As can be seen, both types of data compare very favourably, being the evolution of the wave height and mean water level accurately captured by the model seaward, over and leeward of the structure. As further commented on, the simulated waves break over the crest for both breakwater geometries, with a wave height in breaking approximately 1.2 times the incident wave height.

The middle and lower panels of the two figures present the velocity profiles for the horizontal and the vertical velocity components for each of the different sections. The solid lines represent the numerical results and the dots the measured data. Three velocity profiles are included in each of the plots corresponding to the maximum negative and positive velocities phase-averaged over 10 waves and the velocity averaged over a wave period.

The velocity profiles, in terms of magnitude and shape, are, as expected, very similar on the seaside slope of the breakwater for both values of crest width.

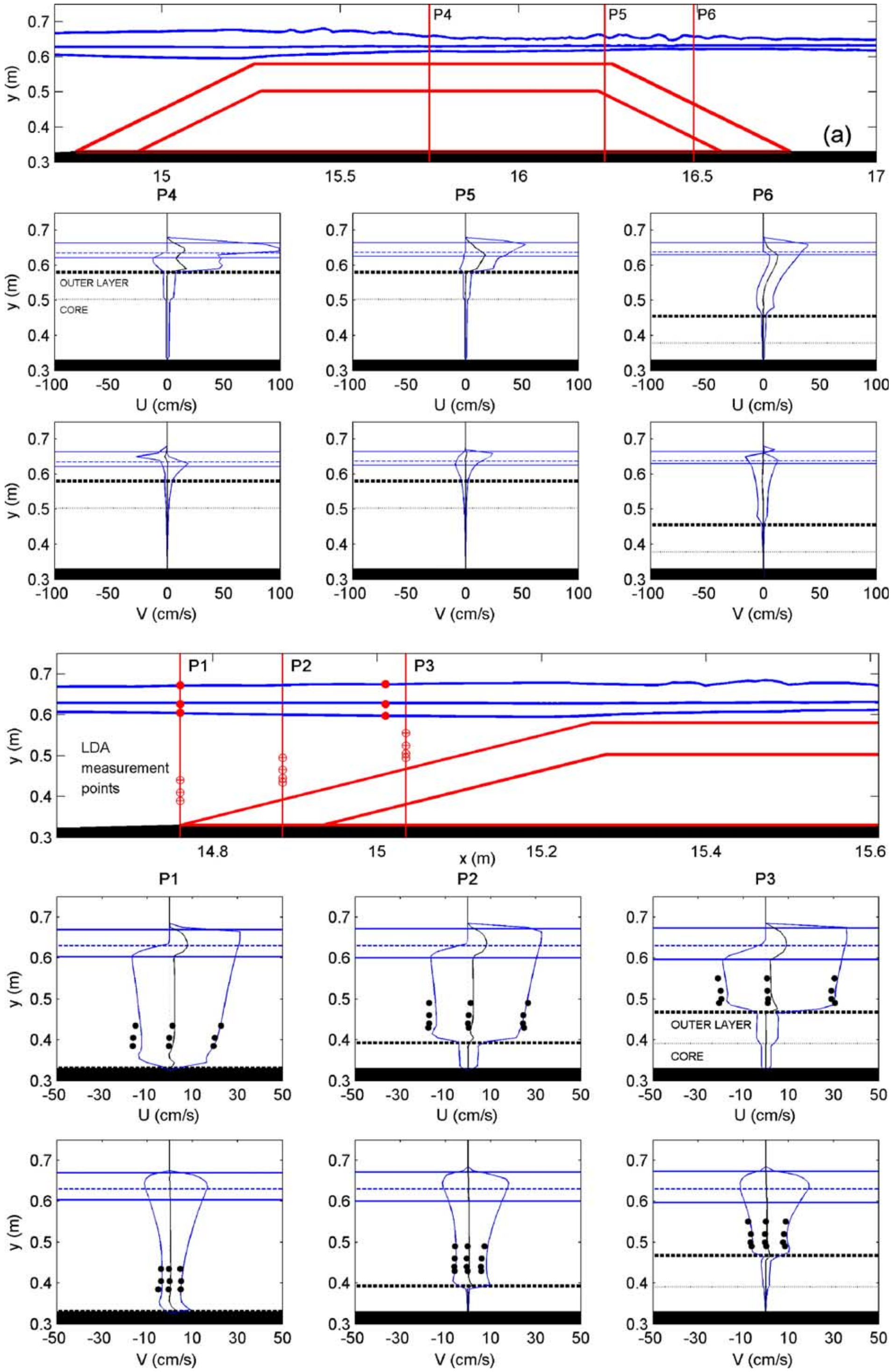

Fig. 1. Phase-averaged velocity profiles at the structure vicinity. $F=-5$ cm, $T=1.6$ s, $H=10$ cm, $b=100$ cm. Dots: experimental data. Solid lines: numerical results. U: horizontal velocity; V: vertical velocity.

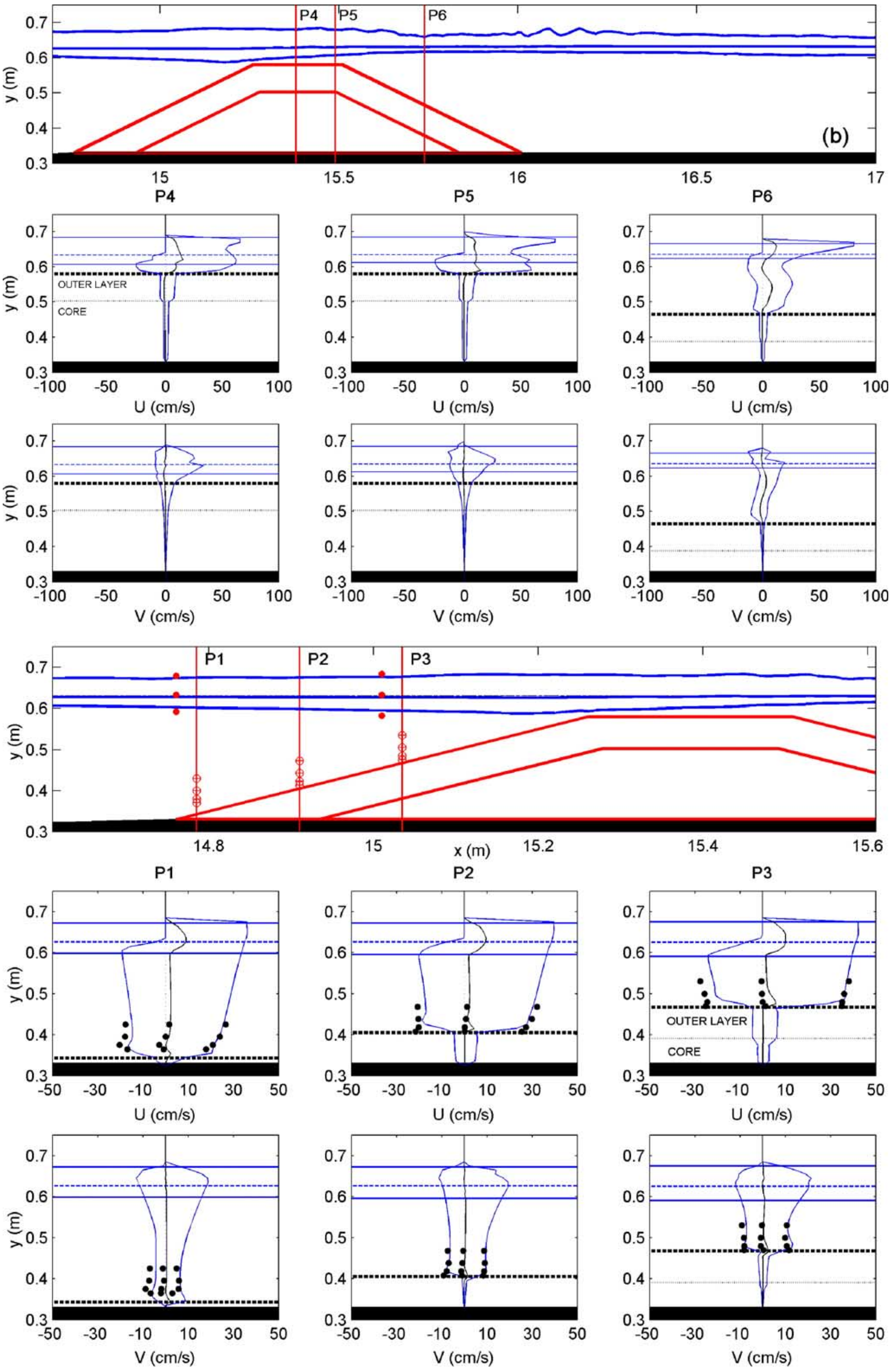
P4
P5
P6
(b)
y (m)
0.3
0.4
0.5
0.6
0.7
15
15.5
16
16.5
17
P4
P5
P6
OUTER LAYER
CORE
U (cm/s)
V (cm/s)
-100
-50
0
50
100
P1
P2
P3
x (m)
14.8
15
15.2
15.4
15.6
P1
P2
P3
OUTER LAYER
CORE
U (cm/s)
V (cm/s)
-50
-30
-10
10
30
50

The flow is fundamentally horizontal, with maximum horizontal velocities on average more than three times higher than maximum vertical velocities. Reflection coefficients have been calculated using the method by Mansard and Funke (1980) for both the laboratory measurements and numerical simulations, with comparable results for both crest configurations. Reflection coefficients for the wide-crested breakwater are 14.3% for laboratory data and 16.7% for numerical simulations, and 16.4% and 18.6% for laboratory data and numerical simulations respectively for the narrow-crest breakwater. That means that the energy reflected by the breakwater is rather similar for both configurations. However, the flow pattern observed on the crest and in the leeside is completely different. A spectral analysis of wave records at both sides of the breakwater has established that the transmission coefficient is about 30% in the case of the $b=100$ cm structure, while it is more than 55% for the $b=25$ cm one. For the same value of structure freeboard ($F=-5$ cm), the short-crested breakwater is confirmed to be less efficient as a wave load dissipater.

Energy is damped in a higher amount in the wide-crest configuration because of the wave breaking over the crest. Larger velocities have been obtained for both geometries at sections 2 and 3, especially above the trough level, revealing a breaking event. In the case of the narrow-crest structure, the profile shape in the upper part of the slope is more complex, affected by breaking-induced vortex structures as will be shown later. As a consequence of the lower energy dissipation in the crest region in the case of the narrow-crest structure, larger velocity values are observed in profile 4, especially above the trough level. The amplitude of the transmitted wave leads to larger values of particle velocity, as the plotted wave amplitude in the upper panel of the figure reveals.

In the case of the wide-crest structure simulation, used for calibration of the model, the calculated maximum velocities errors are less than 7%. Higher errors exist in the case of the narrow crest, but the obtained results are also satisfactory taking into account that no modifications of the calibration parameters have been made. A better agreement could be obtained adjusting the porous flow parameters to the new structure geometry, but these parameters were kept constant for the different simulations in order to test the reliability of the numerical model as a predictive tool.

The highest discrepancies between experimental and numerical results are observed near the boundary, due to the local effects associated with the stones of the armour layer. Wake generation and fine scale turbulence close to the armour stones are not considered by the model. Therefore, an important shortcoming in the computation is the discretisation of the porous material–fluid interface leading to differences between the local measurements and the computational values. It is to be noted that the measurement points are between 2 and 4 cm closer to the structure for the test on the short crest compared to the equivalent test on the wide crest, which may contribute, for the aforementioned reason, to the lower agreement achieved between experimental and numerical data for that test. The maximum error in the maximum horizontal velocities estimation is about 10%, excluding the closest point from the boundary for all the measurement profile.

Fig. 3 presents numerical results of the spatial distribution of the maximum particle velocities evaluated over 10 waves. Peak values near the surface, corresponding to wave breaking and further propagation of the broken wave, and local secondary peaks at the interface of the structure can be observed. The location of the velocity peak values at the free surface can thus be regarded as a hint for the identification of the breaking point, located in the present simulations near the $x=15.5$ m horizontal coordinate for both cases. This result is confirmed considering the numerical data of free surface displacement (validated with laboratory measurements at several locations of the structure's vicinity) and taking the maximum water surface elevation as the breaking criterion.

The near-field velocity pattern evidences the differences between the two distinct breakwater geometries in the post-breaking flow conditions. In Fig. 3 the propagation of the bore along the crest can be observed, till the wave reforms in the transmission zone.

For $b=0.25$ m (Fig. 3b), the velocity map allows a better visualisation of the local maxima at the inner

Fig. 2. Phase-averaged velocity profiles at the structure vicinity. $F=-5$ cm, $T=1.6$ s, $H=10$ cm, $b=25$ cm. Dots: experimental data. Solid lines: numerical results. U: horizontal velocity; V: vertical velocity.

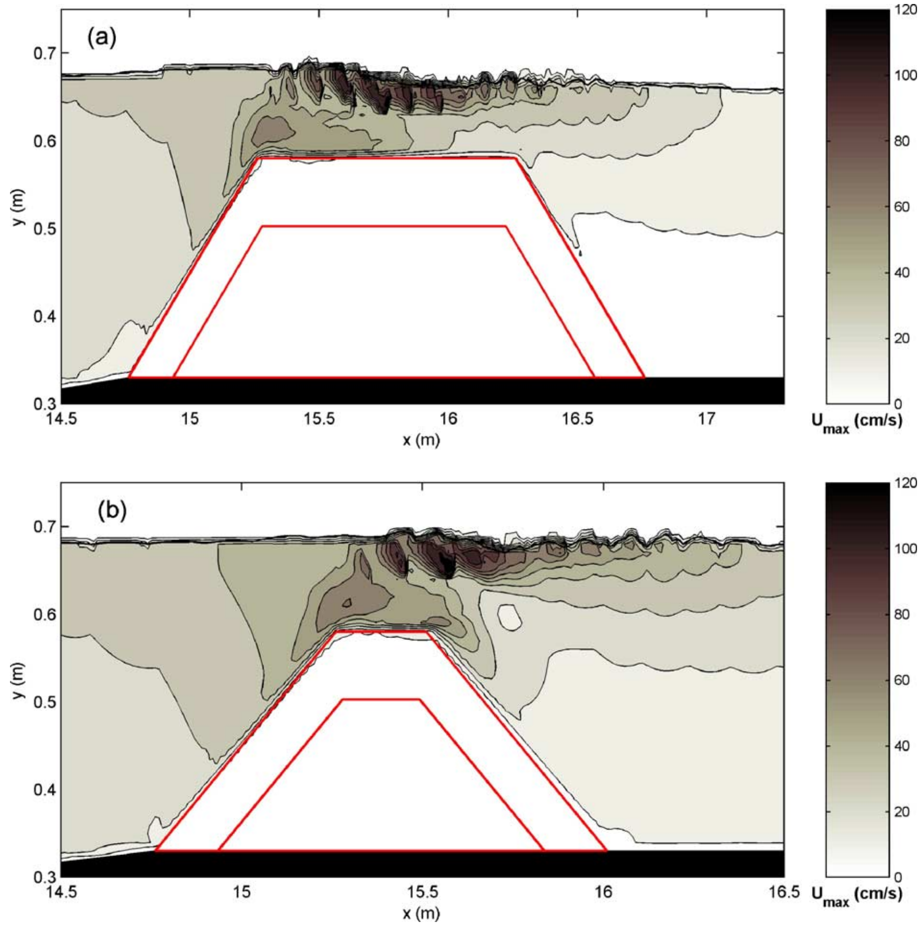

Fig. 3. Computed phase-averaged maximum velocity field. $F = -5$ cm, $T = 1.6$ s, $H = 10$ cm, (a) $b = 100$ cm, (b) $b = 25$ cm.

edge of the crest and upper part of the leeside slope commented earlier. Such a map provides information on the potential vulnerability of the different zones of the structure, with armour stones of the leeside slope seen to be more likely to move downward in the case of the short-crested structure.

Using the velocity data provided by COBRAS an analysis of the time-averaged mean flow around the breakwater has been carried out. Fig. 4 presents the spatial distribution of the mean flow pattern at the lee side of both the wide- and short-crested structures. The current pattern is very similar to what can be observed in 2DV at the central section of a 3D detached overtopped rubble-mound breakwater, with a strong onshore current above the crest due to flow constriction and wave breaking and formation of vortex cells leeward of the structure. This nature-like hydrodynamic behaviour is made possible due to the flow recirculation system, included in both the experimental and numerical wave flume, as shown in Garcia et al. (2004). As LCS are by definition strongly overtopped structures, overtopping produces a set-up leeward of the structure that gives rise in real beaches to three-dimensional current systems. In 2-D configurations the structure overtopping results in a water piling-up in the transmission zone (Loveless et al., 1998) that heavily affects the flow conditions near the submerged structure (Garcia et al., 2004). The flow recirculation mechanism is essentially aimed to prevent such a water piling-up and to allow realistic conditions of flow at the low-crested structure. As can be seen in the figure, the mean velocities at the leeside slope of the short-crested breakwater differ substantially from the wide crest geometry pattern. High

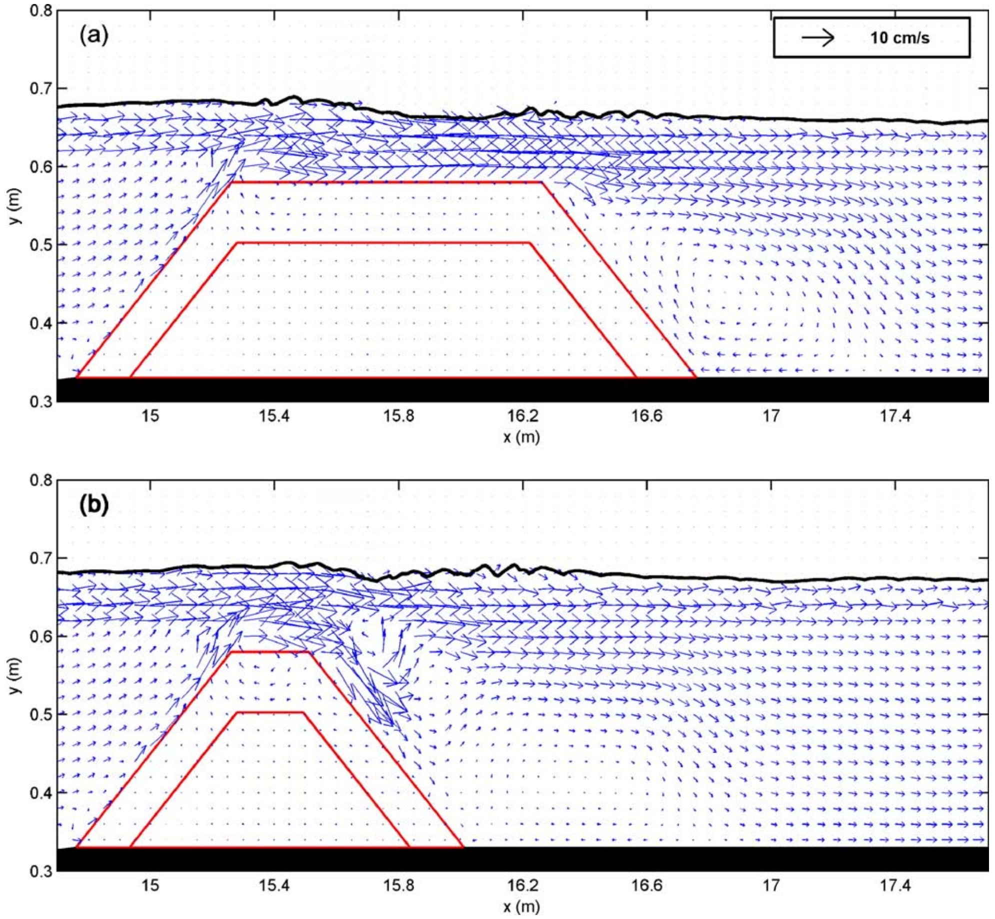

Fig. 4. Computed time-averaged velocity field. $F=-5$ cm, $T=1.6$ s, $H=10$ cm, (a) $b=100$ cm, (b) $b=25$ cm.

values of mean velocities directed downslope can be observed in the higher middle part of the slope, with the subsequent possible influence on rock stability and on the settlement of marine communities.

2.3.2. Peak velocity and turbulence fields around and inside the LCS small-scale model

Valuable information can be extracted from the turbulent intensity distribution around the LCS for a comprehensive structure design including ecological effects. Fig. 5 shows six snapshots of the numerical simulation of 15 cm waves of 1.6 s period with the submerged LCS ($F=-5$ cm), including turbulent intensity and velocity fields both around and inside the permeable structure. Turbulent intensity is defined as $u=\sqrt{2k}$, where k is the computed turbulent kinetic energy (TKE). This parameter is an estimation of the velocity increase due to the turbulent fluctuations. It is observed that turbulence levels are higher on the crest of the broken wave, as could be expected. The numerical model is able to reproduce the turbulence processes associated with wave breaking over the LCS, showing how turbulence is spread onshore by the bore over the crest of the structure. On the leeward side of the structure, turbulent intensity is smaller because turbulence production decreases in the region of the wave crest.

Turbulent intensities are also calculated within the LCS. Higher values are observed at the interface for the outer layer because of the local velocity enhancement due to flow constriction. A larger vertical velocity gradient is developed at the interface, yielding higher turbulence levels. This feature is well predicted by the present model, suggesting that the turbulence

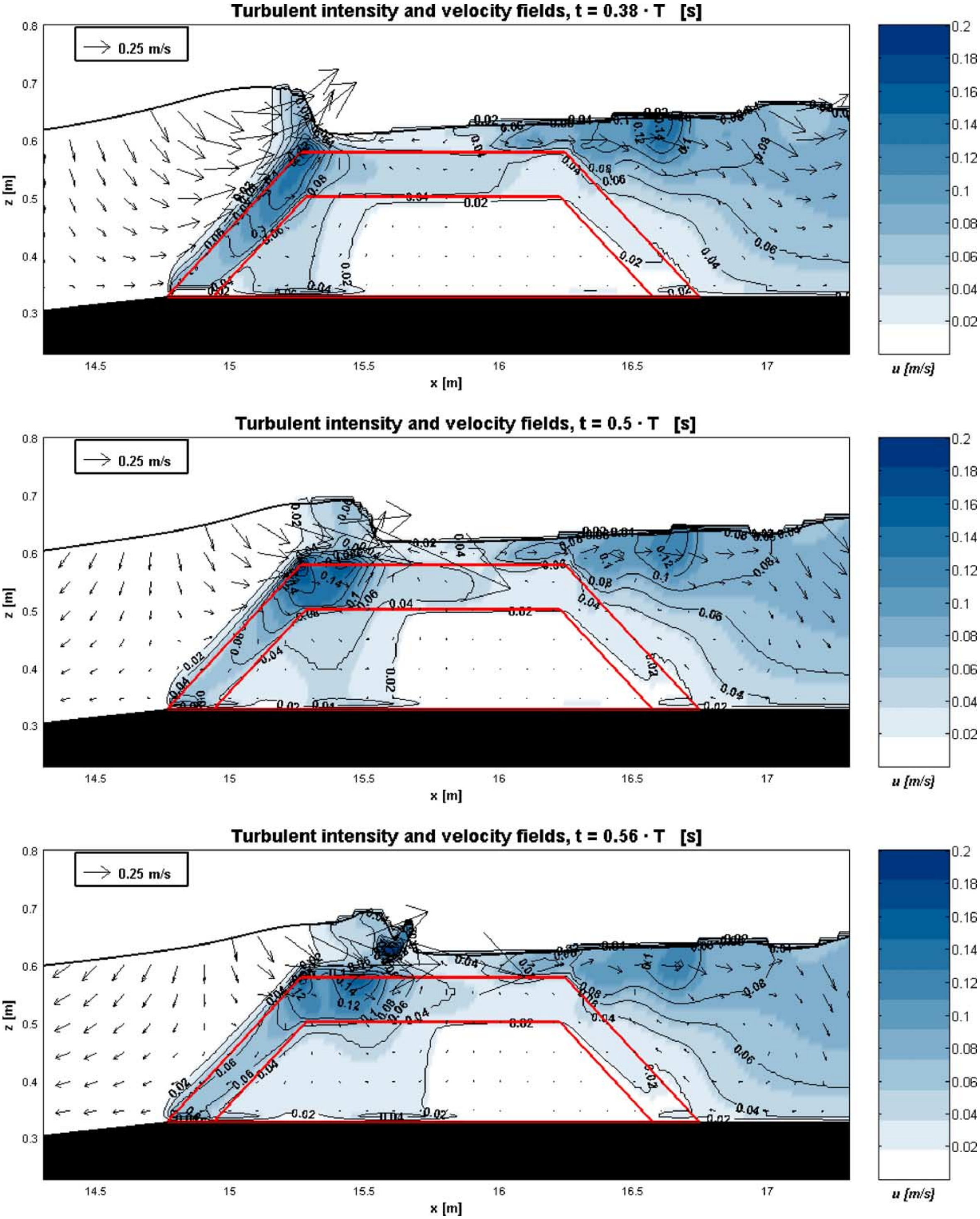
Turbulent intensity and velocity fields, t = 0.38 · T [s]

Turbulent intensity and velocity fields, t = 0.5 · T [s]

Turbulent intensity and velocity fields, t = 0.56 · T [s]

Fig. 5. Simulated turbulent intensity and velocity fields around the structure. Contour lines of turbulent intensity have intervals of 0.02 m/s. $F = -5$ cm, $T = 1.6$ s, $H = 15$ cm, $b = 100$ cm.

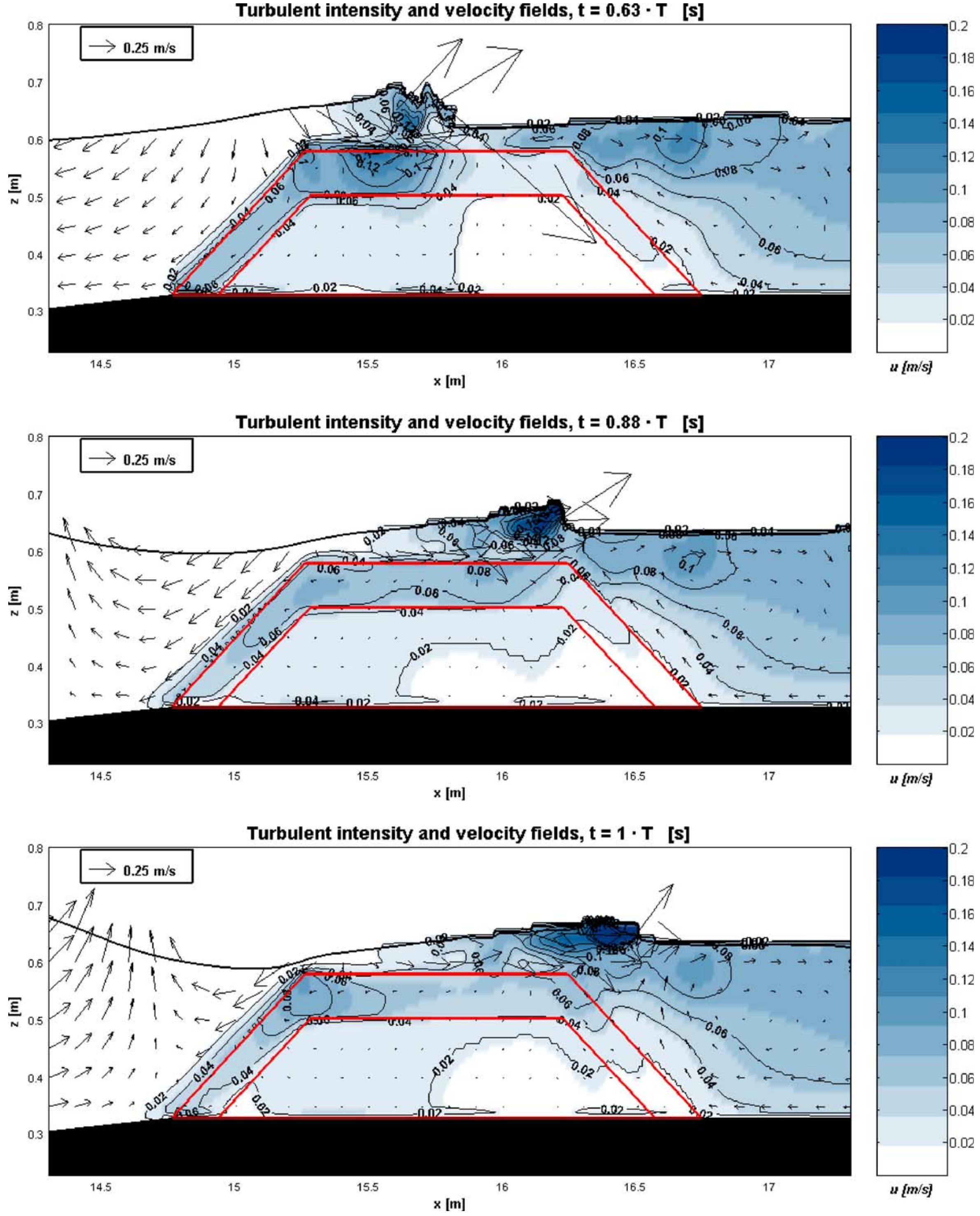
Turbulent intensity and velocity fields, t = 0.63 · T [s]

Turbulent intensity and velocity fields, t = 0.88 · T [s]

Turbulent intensity and velocity fields, t = 1 · T [s]

Fig. 5 (*continued*).

model inside the porous media is qualitatively correct. Maximum values are observed before breaking, when the impinging wave reaches the seaside slope of the structure, as can be seen at $t=0.38$ T and $t=0.5$ T with values of u around 0.16 m/s at the seaside vertex of the structure. The maximum pore Reynolds Re_{p} during one wave period in the outer layer is about 6000. On the other hand, very small values are simulated inside the core for the whole wave cycle. Values not larger than 0.05 m/s are calculated, corresponding to a maximum pore Reynolds number in the breakwater core of approximately 600.

To investigate the role of wave breaking in the near field of the LCS, shear stresses, turbulence production and dissipation mechanisms are examined hereafter. Several magnitudes directly computed by the model are shown in Fig. 6. The shear stresses contribution due to the mean velocity gradients mean rate of strain $\left(\tau_{xz}=\frac{1}{2}\left(\frac{\partial U}{\partial z}+\frac{\partial W}{\partial x}\right)\right)$, where U and W are Reynolds averaged horizontal and vertical velocity), the turbulent shear Reynolds stresses defined as $\tau^{*}_{xz}=-<u'w'>$, the turbulent dissipation rate (ε) and the main contribution term to the TKE production ($\tau^{*}_{xy}\partial U/\partial z$) are plotted. The presented results correspond to incident wave height and period of 15 cm and 1.6 s respectively. In order to compare mean and turbulent contribution to the shear stresses, τ_{xy} and τ^{*}_{xy} are plotted using the same colour scale.

In the first four panels ($t=0.5$ T), the impinging wave is about to break. The gradient of vertical velocity increases over the LCS due to the velocity damping inside the porous media. At the interface, shear stresses increase, yielding turbulent generation. This can be seen in the turbulent production panel ($\tau^{*}_{xy}\delta U/\delta z$), where black patches can be observed at the top seaside part of the structure. The mean shear stress (τ_{xy}) is larger than the turbulent shear stress (τ^{*}_{xy}), revealing that the velocity gradient at the fluid–structure interface is the most important turbulent production source before wave breaking occurs. The turbulent dissipation rate (ε) presents larger values inside the outer layer, showing a stronger turbulent regime than expected within the core. Most of the TKE is dissipated inside the porous media, and a small part at the interface. However, most of the TKE is generated just at the outer layer interface.

The lower four panels in Fig. 6 correspond to the breaking wave propagation over the crest of the breakwater. Additional turbulent production–dissipation mechanisms are present and related to wave breaking. Turbulent production regions are easily identified at the wave crest and at the crest of the structure. Dissipation occurs in the region of the wave crest and within the outer layer. Calculated turbulent shear stress increases at the wave crest, but remains very similar to the pre-breaking wave conditions (first four panels). This reveals that the contribution of the turbulent shear stress to the total shear stresses is important only in the vicinity of the breaking point. Around the structure, the contribution of the turbulent shear stress is poor.

The knowledge of the shear stress distribution is of high relevance for assessment of the structure stability. The information provided by the numerical model shows that the armour stones forming the crest are likely to be displaced by the breaking waves due to the large values of the shear stress, with the maximum values being reached at the seaside vertex.

As an example of application of the model in support to ecological studies conducted in the frame of the DELOS project, numerical results of the ratio $U_{\mathrm{MAX}}/\sqrt{2gH_{\mathrm{b}}}$ are presented in Fig. 7 for 10 cm and 15 cm incident waves (respectively upper and lower panels), being U_{MAX} the maximum value of horizontal velocity computed in a wave period. The black lines over the structure represent the upper and lower envelopes of wave height and the mean water level.

$U^{*}=(2gH_{\mathrm{b}})^{1/2}$, with H_{b} the wave height at the breaking point, is a commonly used maximum velocity parameter for assessment of marine communities settlement (Denny, 1988). This expression has been derived on the assumptions that the maximum water velocity associated with a breaking wave is roughly equal to the velocity of the particles at the crest of the breaking wave, and that the wave breaks at a water depth equal to the wave height. The breaking point in the numerical computations has been defined as the location where the upper wave height envelope reaches its highest value.

The numerical results reveal that $U_{\mathrm{MAX}}/\sqrt{2gH_{\mathrm{b}}}$ increases with the incident wave height. The distribution patterns of the highest velocities are very similar in both cases, with the maximum values computed at the offshore part of the crest. In the case of the 15 cm waves, these maximum values are about 10% larger

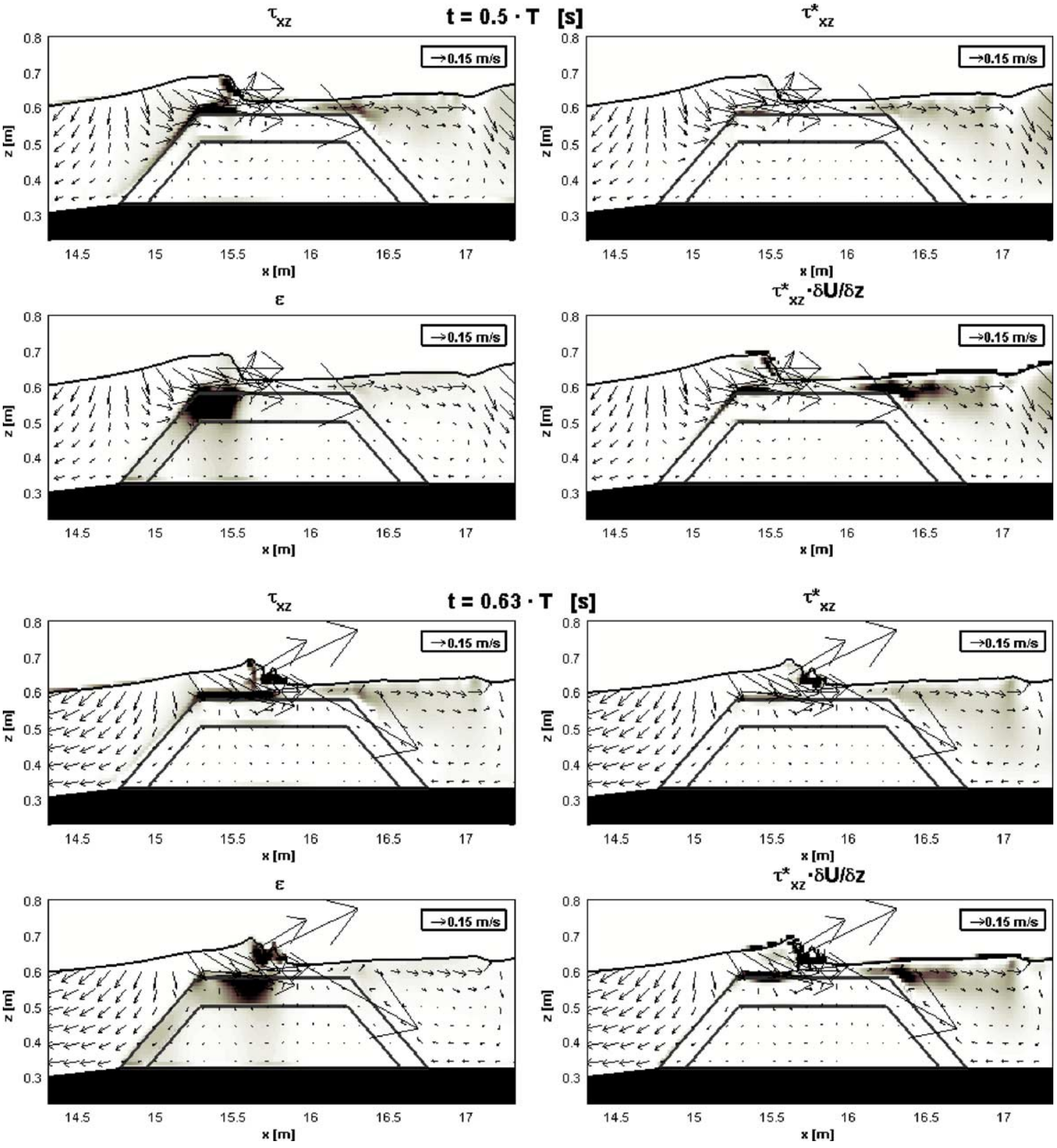

Fig. 6. Simulated shear stresses components (τ_{xz} and τ^*_{xz}), turbulent dissipation rate (ε) and turbulent kinetic energy production term ($\tau^*_{xz}\,\delta U/\delta z$). Black colour represents larger values. $F=-5$ cm, $T=1.6$ s, $H=10$ cm, $b=100$ cm.

than for the smaller incident wave height. The presented results show that the empirical formulation presented by Denny (1988) tends to overestimate the maximum velocity around the structure in both cases. The numerical model predicts values of maximum velocity about 50% smaller than those obtained from Denny (1988).

3. Three-dimensional modelling using an LES approach

3.1. Introduction

Even if some of the general foundations and features of the three-dimensional model herein

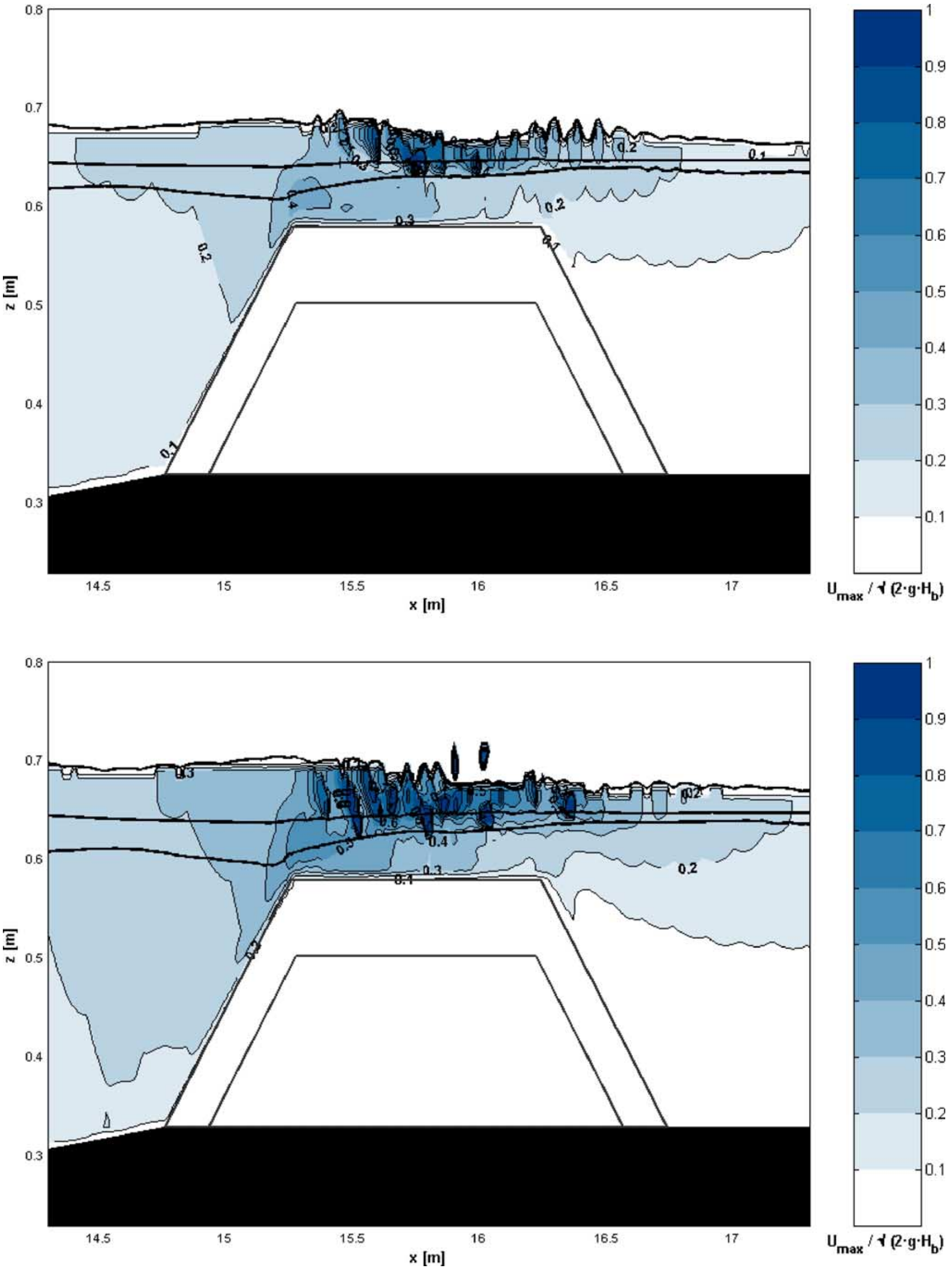

Fig. 7. $U_{\mathrm{MAX}}/\sqrt{2gH_{\mathrm{b}}}$ ratio for $H=10$ cm (upper panel) and $H=15$ cm (lower panel). Contour lines of velocity have intervals of 0.01.

described are similar to those of the Mayer and Madsen (2000) model, the main differences are due to space discretisation and the way turbulence is solved.

In this new model, the Navier–Stokes solver solves the instantaneous Navier–Stokes equations in three dimensions. The spatial discretisation is based on the finite-volume approach on a multi-block grid.

The time integration of the Navier–Stokes equations is performed by application of the fractional step method.

As explained for the 2-D model, the free surface is resolved using a Volume of Fluid (VOF) description. However, in the present model, the method described in Hirt and Nichols (1981) is improved with a new scheme for the advection of the conservative quantity *F*, see Ubbink (1997). The grid is fixed, while the conservative quantity *F* moves with the fluid. *F* is assigned a value of 1 within the fluid domain and 0 in the void domain (the effect of air is not included). $F=0.5$ determines the position of the surface. At the surface, setting the pressure equal to the atmospheric pressure fulfils the dynamic boundary condition. The kinematic boundary condition is included by extrapolation of the velocities within the fluid domain to the surface.

The waves are generated at an inlet boundary where Stokes waves up to 5th order, cnoidal waves up to 5th order or stream function waves can be specified. At the beach, the remaining wave energy is absorbed by means of a sponge layer.

The 3D Navier–Stokes solver includes several turbulence models: RANS (Reynolds Averaged Navier–Stokes equations) models such as k–ε, k–ω or LES models (Large Eddy Simulation) with a Smagorinsky sub-grid scale model or a k-equation for the sub-grid scale turbulence.

In the study of submerged breakwaters a rather simple approach, which will be described in detail below, has been used in order to reduce the computational time and complexity. Further the breakwater was modelled as impermeable, which is a simplification of the experiments where the breakwater was permeable. The study of overtopping of short crested low-crested breakwaters is only influenced by the turbulence to a minor degree, whereas the transmitted wave can be affected by the turbulence generated inside and along the surface of the low-crested structure. The turbulence will affect the shape of the return flow to some degree, while the turbulence will have a small effect on integrated flow rate through the gap. As it is the flow rate over and through the gap that is of main interest of the full 3D study, the simplifications are acceptable. In the following a detailed description of the LES model is presented.

3.2. The subgrid model for Large Eddy Simulation (LES)

The basis for the Large Eddy Simulation is the spatial filtering of the Navier–Stokes equations. Using a top-hat filter the grid can be used as the filter itself. This is the most common way of filtering when the solution method is based on the finite volume method. The velocity scales smaller than the grid can naturally not be simulated anyway. The following equation summarises the filtering process for the momentum equation:

$$\rho\frac{\partial\overline{u}_i}{\partial t}+\rho\frac{\partial\overline{u_iu_j}}{\partial x_j}=-\frac{\partial\overline{p}}{\partial x_i}+\frac{\partial}{\partial x_j}\mu\left(\frac{\partial\overline{u}_i}{\partial x_j}+\frac{\partial\overline{u}_j}{\partial x_i}\right). \tag{1}$$

In Eq. (1), the second term on the left hand-side has to be split up in a part that can be simulated directly:

$$\frac{\partial\overline{u_iu_j}}{\partial x_j}=\frac{\partial\overline{u}_i\overline{u}_j}{\partial x_j}+\left(\frac{\partial\left(\overline{u_iu_j}-\overline{u}_i\overline{u}_j\right)}{\partial x_j}\right). \tag{2}$$

The first part is simulated directly while the second part is moved to the right hand side and has to be modelled. This part is also called the subgrid scale Reynolds stress:

$$\tau_{ij}^{s}=-\rho\left(\overline{u_iu_j}-\overline{u}_i\overline{u}_j\right). \tag{3}$$

Eq. (3) is the closure problem for which we have to use a model. If no model is applied, resolved turbulent kinetic energy can only dissipate due to the physical viscosity and due to artificial numerical viscosity. This will often lead to a too slow dissipation of energy giving too high turbulence levels. Further the artificial numerical dissipation depends on the resolution, the numerical discretisation of the algorithm and is normally not known, which adds uncertainty to the solution. Therefore a clear definition of how the excess energy should be dissipated is important even in cases where the turbulence is not of main interest.

3.2.1. Smagorinsky subgrid model

A number of different subgrid-scale models (sgs-models) have been proposed. Many of these are based on the Smagorinsky sgs-model. This is an eddy visc-

Table 1
Physical model tests used for validation of the NS3

Case	Test #	Berm	Type of spectrum	F (m)	H/L	H (m)	T (s)
1	28	Wide	Regular	0.00	0.04	0.076	1.10
2	38	Wide	Regular	−0.07	0.04	0.103	1.28

osity model that is closely connected to the strain rate and the grid size. The subgrid scale stresses:

$$\tau_{ij}^{s} = -\rho\left(\overline{u_i u_j} - \overline{u}_i\overline{u}_j\right) \tag{4}$$

are modelled in the following way:

$$\tau_{ij}^{s} - \frac{1}{3}\tau_{kk}^{s}\delta_{ij} = 2\mu_t\overline{S}_{ij},\ \overline{S}_{ij} = \frac{1}{2}\left(\frac{\partial\overline{u}_i}{\partial x_j} + \frac{\partial\overline{u}_j}{\partial x_i}\right). \tag{5}$$

The eddy viscosity is found according to:

$$\mu_t = \rho(C_{\mathrm{s}}\Delta)^2|\overline{S}| \tag{6}$$

where Δ is the filter length scale and $|\overline{S}| = \left(2\overline{S}_{ij}\overline{S}_{ij}\right)^{1/2}$. C_{s} is the Smagorinsky constant that is in the order of 0.065 to 0.2. The model is rather simple which is an advantage in the computation. However, the optimal value of the Smagorinsky constant varies from flow to flow. For instance close to a wall the Smagorinsky constant can be reduced according to the van Driest damping.

3.3. Validation of the model

As presented in Table 1, two conditions were selected for the validation of the 3D Navier–Stokes solver (NS3). Regular wave conditions were applied in both tests. Zero freeboard was used in case 1, while a submerged structure was tested in case 2. The test # refers to the experimental number performed at Aalborg University as part of the DELOS project.

In the set-up of NS3 the symmetry in Layout 1, see Kramer et al. (2005—this volume) Fig. 7, has been used to reduce the number of computational cells needed to resolve the submerged breakwater and rip channel. The computational domain was resolved with a total of 589,824 computational cells. Along the x-axis (from the wave-maker towards the beach) 256 cells were used. In the transverse direction and vertical the number of cells was 96 and 24, respectively.

The structures were represented as impervious in NS3, and no reflection of waves from the beach behind the structures was allowed in the model. A Large Eddy Simulation (LES) approach was applied to simulate the effect of turbulence below the grid scale. The Smagorinsky sub-grid scale model was applied. The turbulence model is rather simple, since its main purpose is to dissipate the transformed wave energy in a reasonable manner. Fig. 8 presents a snapshot of the instantaneous free surface as calculated by NS3 for the conditions in case 1. Please note that advantage has been taken of the symmetry in Layout 1 to limit the area covered by the model to half of the basin.

A comparison between instantaneous free-surface levels calculated by NS3 and the corresponding

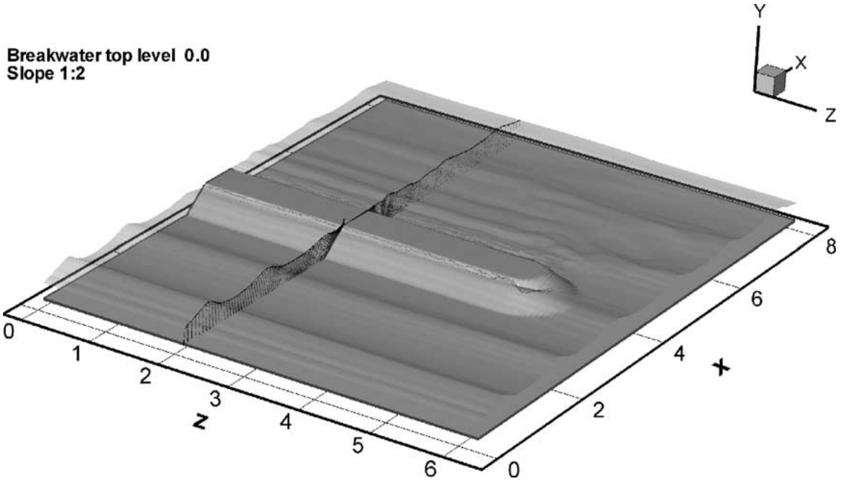

Fig. 8. Instantaneous free surface as calculated by NS3.

records during Test 1 is presented in Fig. 9 at different locations (wave gauges) within the basin. Please note that the NS3 model was used to simulate the first 30 s of the test, after the wave generator paddles had been activated. As Fig. 9 shows, there is a very good agreement between measured and calculated values in front and on top of the structure, both with regard to amplitude and phase of the signals. The agreement is not so good at the position of gauge 18, possibly due to reflections from the absorbing beach and percolation in the structure in the physical model; these effects are not accounted for in NS3. Another reason for the observed discrepancy could be the high turbulence levels, which have not been sufficiently dissipated by the subgrid scale model.

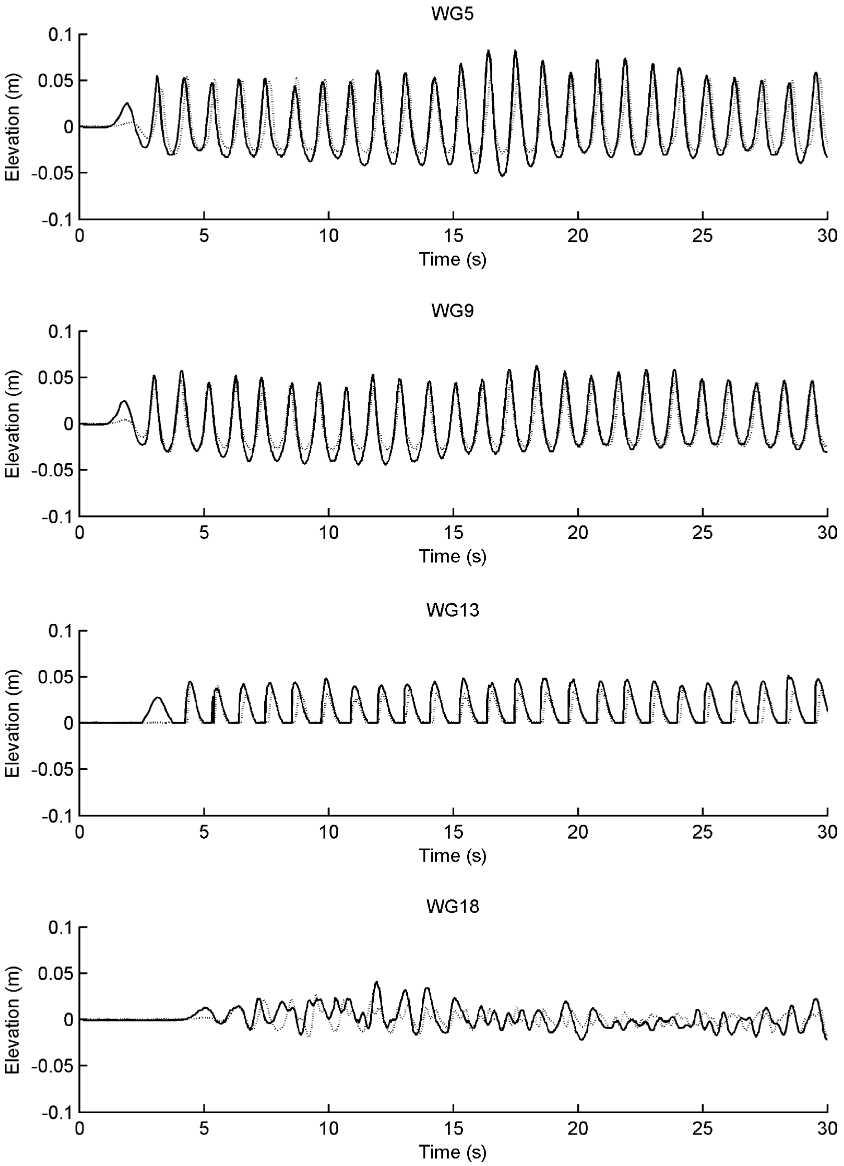

Fig. 9. Calculated (full line) and measured (dashed line) instantaneous free surface in front, on top and behind the structure in case 1. From top to bottom: wave gauges 5, 9, 13 and 18, cf. Fig. 7 in Kramer et al. (2005—this volume).

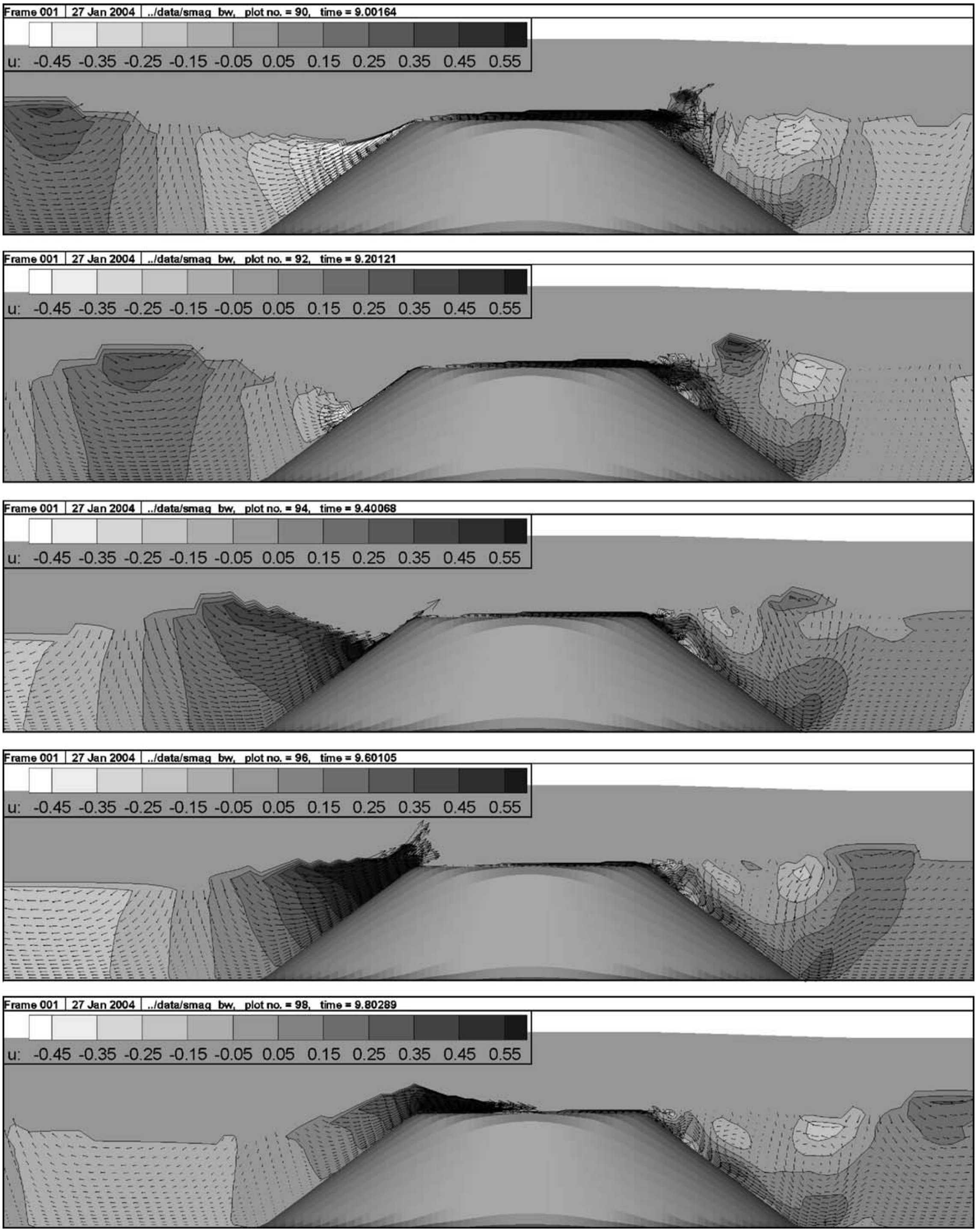

Fig. 10. Example of the flow over the breakwater, test case 28, during over wave period at $z = 2$ m cf. Fig. 8.

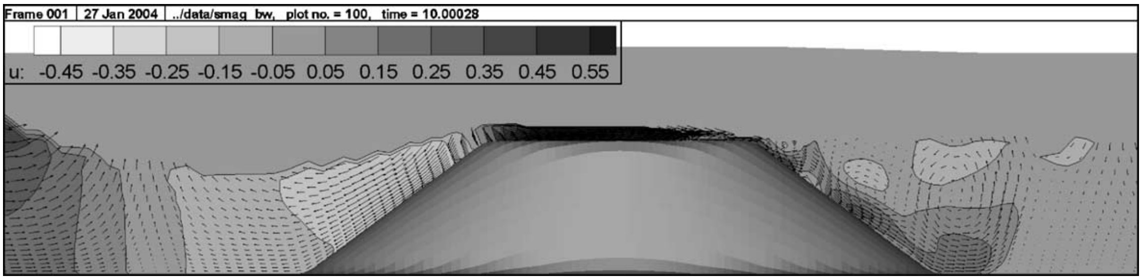

Fig. 10 (*continued*).

Fig. 10 displays transects to the breakwater in $z=2$ m as shown in Fig. 8. Results show that the flow field is almost periodic in front of the breakwater, while the flow field is more chaotic on the lee side leading to production of turbulence. The comparison between the modelled and measured water levels was in good agreement in front and on the top of the breakwater while the comparison on the lee side was not that clear.

An example of the depth integrated velocity field is given in Fig. 11. Even though the freeboard is rather small, actually 0 compared with respect to the still water level, the depth averaged velocity out through the rip channel is in the order of -0.25 m/s. This is in the same order of magnitude as the maximum particle velocities under the wave. At the breakwater head the flow is either small or directed towards the beach.

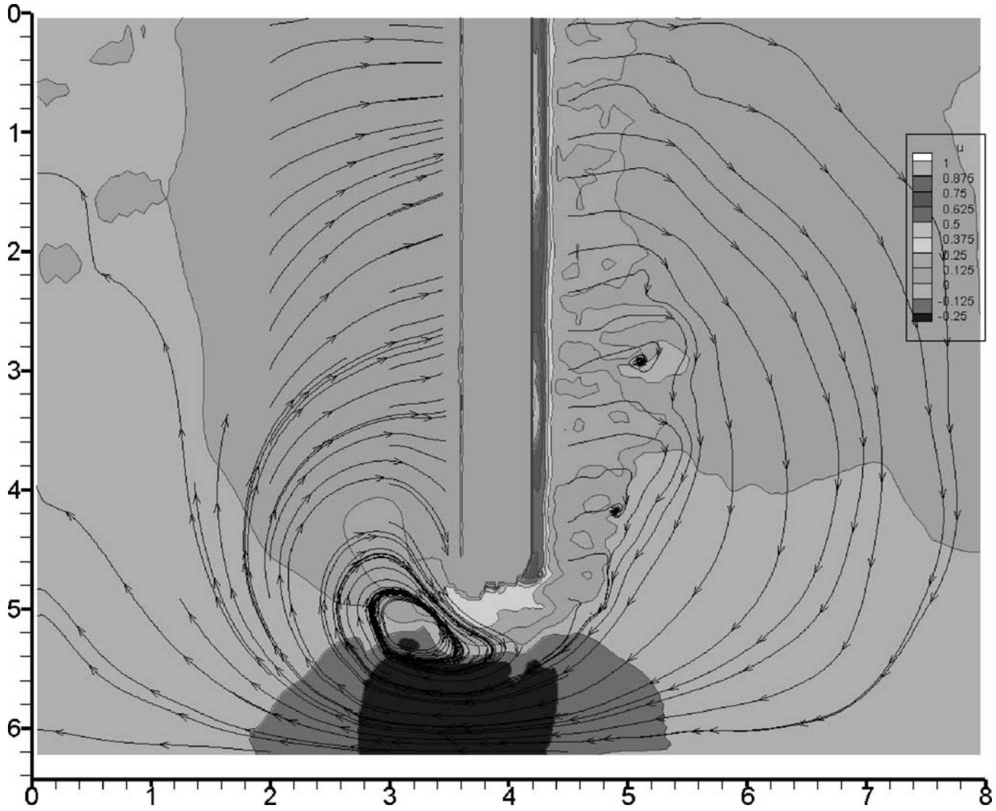

Fig. 11. Depth integrated flow field and time averaged flow field at 25 wave periods from the beginning of the simulation.

Thereby a very strong eddy acts on the offshore part of the head of breakwater.

4. Conclusions and future work

In this paper, a description of the progress achieved within DELOS on our knowledge on the processes and modelling involved in wave interaction with LCS is presented. Most of the work has been devoted to the numerical modelling of the effects of the breaking process on the functional design as well as on the velocity and turbulence distribution around and inside LCS.

The numerical work has been based on two different numerical models originating from the Navier–Stokes equations: a two-dimensional model based on the Volume-Averaged Reynolds Averaged Navier–Stokes (VARANS) equations named COBRAS and a three dimensional model based on a Large Eddy Simulation (LES) approach, named NS3.

The first model has the limitation of considering only two-dimensional flows and the problems associated with the possible shortcomings of using k–ε equations for turbulence modelling. However, it has several advantages. It is able to simulate porous flow including turbulence in the permeable region and it requires less computational resources which permits the evaluation of the functional performance of LCS under several wave incident conditions, structure geometry and porous material characteristics. To date, models based on two-dimensional RANS approximations are possibly the best suited to study wave and LCS interaction for engineering purposes, since computational efforts are reasonable and the number of simplifying assumptions is considerably reduced compared to other existing models.

The second model has the advantage of being able to reproduce three dimensional processes including a better turbulence description based on an LES approach. Large Eddy Simulation (LES) solves the largest scale motions of the flow while modelling only the small scale motions. It can be regarded as a kind of compromise between the RANS models and the direct numerical simulation (DNS) in which the Navier–Stokes equations are solved for all the motions in the turbulent flow. In LES, more turbulent motions are computed and fewer approximated than in RANS models. However, the computation time is increased considerably. Furthermore, the presented LES-based model does not include porous flow modelling at this stage and therefore neglects one of the important processed involved in wave and LCS interaction.

As a conclusion, it can be said that, even if it is obvious that in the future the 3-D Navier–Stokes models will be one of the main tools for the modelling of wave interaction with LCS, at this stage of development, the two-dimensional model combined with some 3-D specific applications is probably the most suitable way to carry out the analysis of the flow.

A validation of the two-dimensional model for two crest-widths has been carried out under breaking conditions. The model performs very well, showing very good comparisons with the experimental records of velocity and free surface.

Different flow patterns have been observed for the two different crest breakwater configurations. Reflected energy is similar in both cases. However, transmitted energy is strongly related with the crest width. In the wide crest configuration, most of the energy is dissipated by breaking and a short part is transmitted onshore. Larger velocities have been observed on the crest for both crest configurations. The potential vulnerability regions have been identified studying the maximum velocity values. The seaside vertex for the wide crest breakwater appears as the most exposed region for both configurations.

Turbulent intensity has been computed in the fluid region and within the porous medium revealing weaker turbulence levels within the structure. Larger values have been observed beneath the wave crest after breaking. Turbulence levels within the porous media appear to be larger at the outer layer because of the overshooting at the leeside slope at the crest. Turbulent intensity values are close to zero inside the core. Shear stresses maps show that the mean rate of strain is more important from the rock stability point of view than the turbulent component of the strain rate. Reynolds stresses appear only important in the broken wave crest. Larger shear stress values at the seaside vertex may induce potential rock mobility.

Even with rather simple turbulence models the overtopping of water over the submerged breakwater is predicted quite well. The three-dimensional numerical examples are made with an impermeable wall, and therefore turbulence is not important for the overtopping on the offshore side of the breakwater. On the leeside of the breakwater the flow is more chaotic and turbulent and therefore it is more difficult to achieve a good comparison here. However, in terms of continuity it only affects the distribution of the flow though the rip channel and not the magnitude as that is governed by the overtopping.

Acknowledgements

This study was performed within the framework of the European Union project EVK3-CT-2000-41, Environmental Design of Low-crested Coastal Defence Structures (DELOS).

Appendix A. 2D simulation of regular wave interaction with LCS at prototype scale

In the present section, additional computations performed to test the potential application of the model to a prototype scale are presented. For this purpose, and as a numerical exercise, a characteristic section of the Elmer (UK) detached rubble-mound breakwaters (one of the study sites in the project) has been considered as an example of real LCS geometry. No field measurements of flow data, which would permit to validate the numerical model for assessment of LCS functioning beyond laboratory scales, are available. However, the application of the COBRAS model to wave interaction with low porous breakwaters at a real scale has not been performed to date and should be regarded as an additional step in the process of model exploitation for engineering design purposes.

In the present section, following a brief presentation of the prototype layout on Elmer site and a description of the numerical set-up for prototype simulation, numerical results are presented, with emphasis being placed on the most relevant aspects of the near-field flow conditions for assessment of the ecological impacts of the breakwater.

A.1. Numerical set-up

The numerical set-up designed for the large-scale simulation is inspired from Elmer site layout. As specified in other studies of the present issue, the Elmer coastline sector is located on the southern coastline of England and has been selected as one of the DELOS project study areas. The considered stretch of coast is protected with a segmented offshore breakwater scheme, deployed to aid in the retention of beach fill material. The protection scheme consists of eight parallel structures, with slopes of 1:1.5 and made of blocks of around of 8 tons. The crest elevation is 4.5 m for six of the eight deployed breakwaters and 3.0 m for the other two. The distance from the coastline varies from 38 m to 88 m. The bathymetric

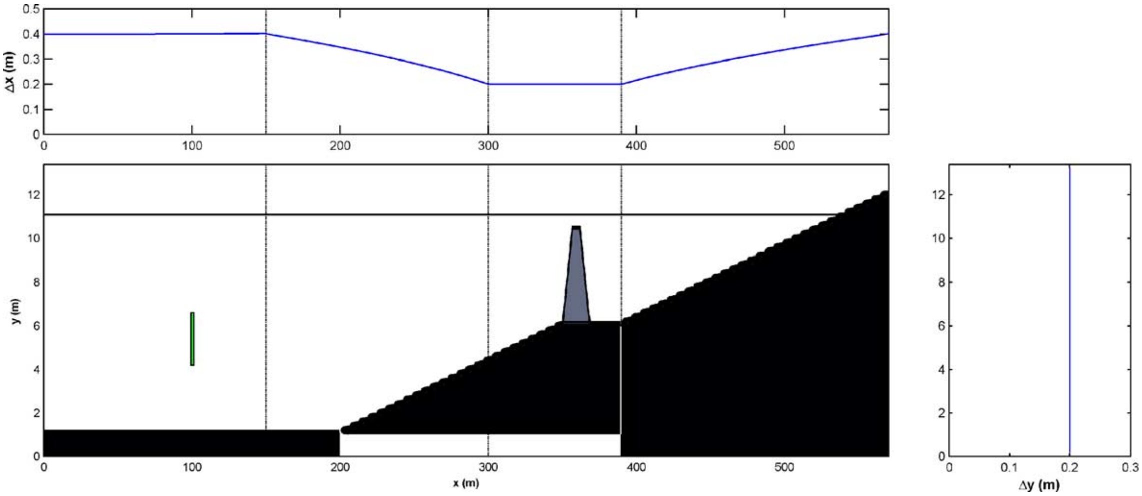

Fig. 12. Numerical domain and grid size distribution for the Elmer LCS prototype case.

configuration of Elmer beach is relatively simple with isobaths running almost parallel to the coastline. The average slope of the beach is 1:50. Elmer site is included in a macrotidal environment, with mean spring and neap tidal ranges of 5.3 and 2.9 m respectively. The breakwaters toe is exposed on all low tides except extreme neap tides. At high tide, the breakwaters do not become completely submerged. However, in the present numerical exercise, as explained below, the considered structure is submerged.

The numerical set-up for the real scale simulation is displayed in Fig. 12. Similarly to the small-scale simulations presented in previous sections, the domain is divided into four regions: wave genera-

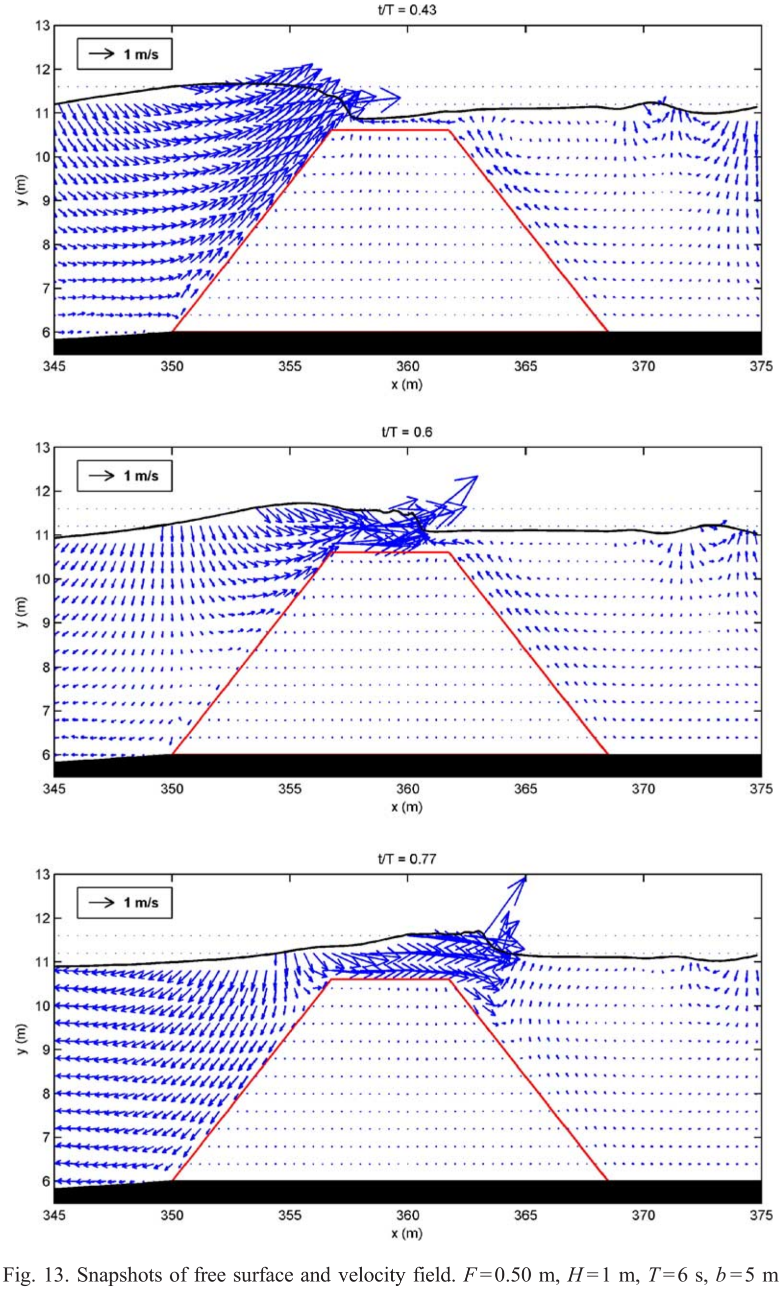

Fig. 13. Snapshots of free surface and velocity field. $F = 0.50$ m, $H = 1$ m, $T = 6$ s, $b = 5$ m.

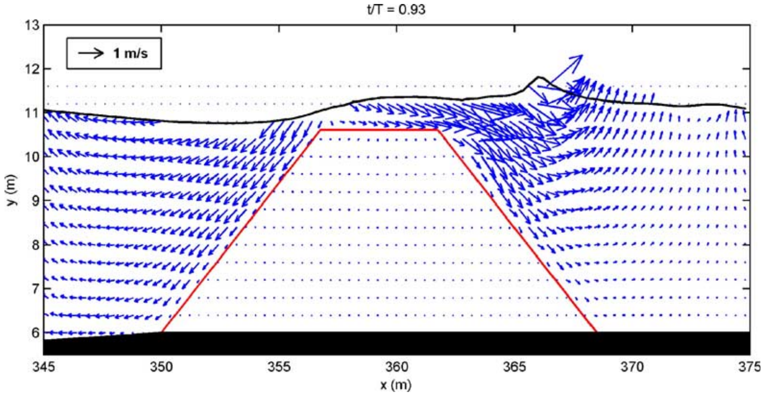

Fig. 13 (*continued*).

tion, wave transformation, structure vicinity and final beach. The length of the computational domain is 570 m × 13.20 m. The grid size is constant in the y-direction, $\Delta y = 20$ cm. The cell dimension varies in the x-direction, being the maximum resolution defined in the vicinity of the structure: $\Delta x = 20$ cm. In the zone of wave generation, the grid size is 40 cm × 20 cm. The total number of cells of the domain is 1925 × 66. Upper and right panels in Fig. 12 display the grid size distribution along the entire mesh in the x- and y-directions.

The studied structure has a 5 m crest width, $1V{:}1.5H$ slopes angle and a 4.5 m total height. The breakwater is homogeneous, made of one single type of rocks. A porous medium with $D_{n50} = 1.44$ m and porosity 0.45 has been defined for simulation of the Norwegian syenite 8-ton blocks used in Elmer. Though the detached breakwaters built in Elmer

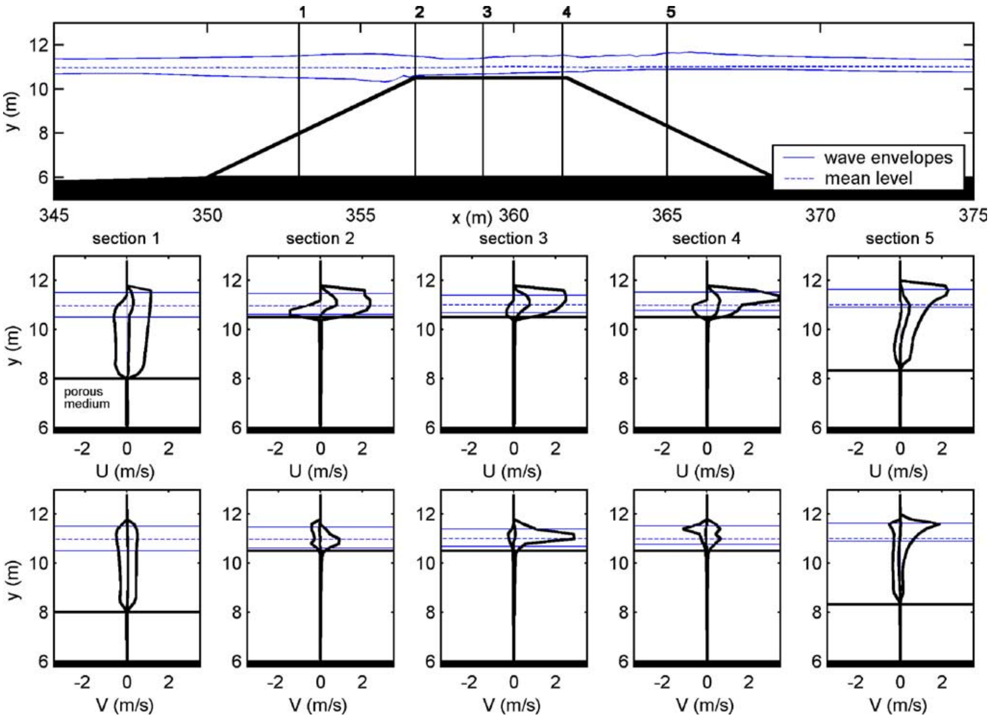

Fig. 14. Maximum, mean and minimum velocity profiles. $F = 0.50$ m, $H = 1$ m, $T = 6$ s, $b = 5$ m.

are low but always surface-piercing, the computations described herein are performed considering slightly submerged structures in order to test the model ability in reproducing the complicated wave-induced flow pattern at slightly submerged permeable obstacles. The depth at the structure toe is set to the fictitious value of 5 m and the structure freeboard −0.50 m. The considered values of freeboard and depths at the breakwater seaward toe correspond to common values of LCS configurations on European coastlines.

The porous flow parameters are set at $\alpha = 1000$ and $\beta = 1.2$, corresponding to the calibration values of the structure core in previous simulations of submerged

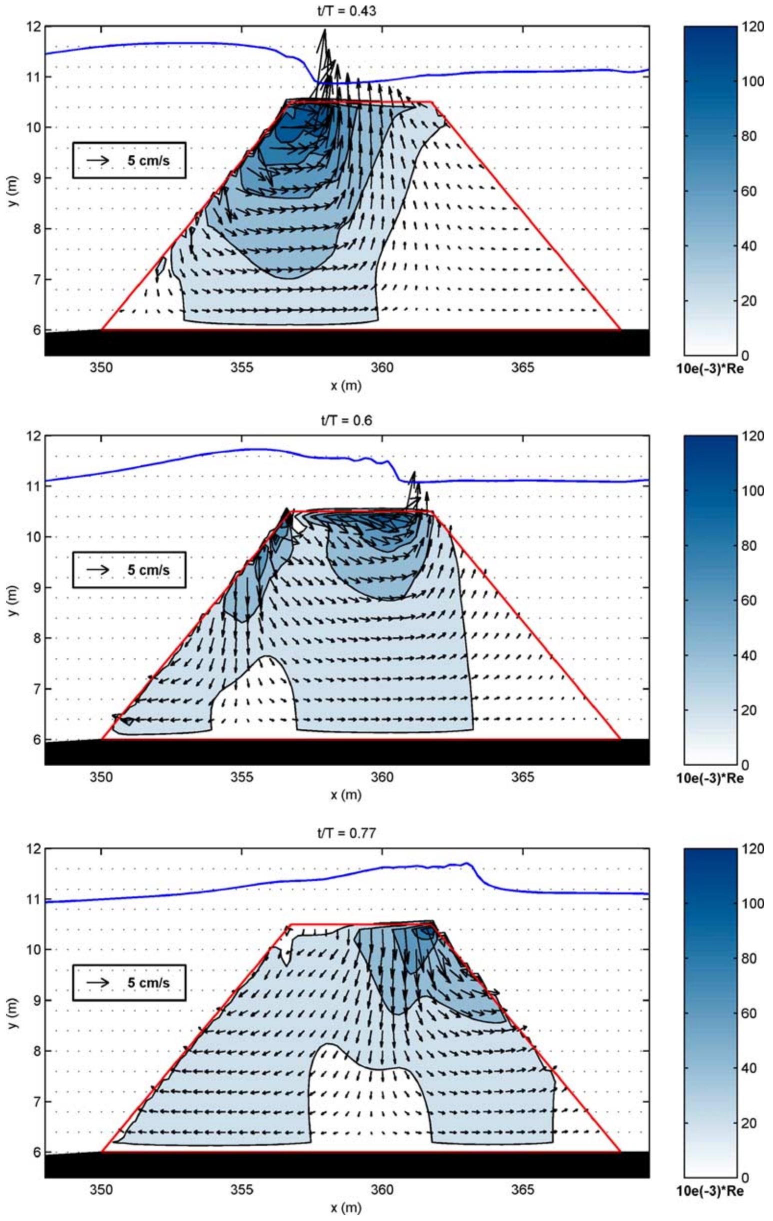

Fig. 15. Snapshots of porous flow velocity field and spatial distribution of pore Reynolds number. $F = 0.50$ m, $H = 1$ m, $T = 6$ s, $b = 5$ m.

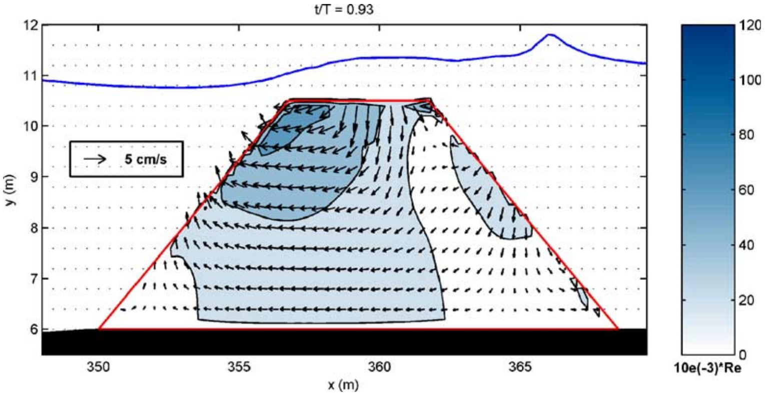

Fig. 15 (*continued*).

breakwaters with COBRAS (see Garcia et al., 2004). In order to simulate the uniform mild sloping-bathymetry of Elmer beach, a uniform 1:30 slope has been included in the numerical domain at both sides of the horizontal segment of the flume bottom on which the structure is defined. The slope of the simulated beach is greater than the real Elmer beach slope so as not to deal with an exaggeratedly wide computational domain.

A.2. Results of the simulation

In this section, results of the simulation of Elmer-type LCS response to regular wave attack and associated near-field flow conditions are presented. The presented results correspond to regular Stokes *V*th order waves of 1 m height and 6 s period, generated at a 10 m water depth. A total of 600 s, i.e. about 100 waves, have been simulated.

A series of snapshots of the phase-averaged velocity field, at different stages of the propagation of 1 m incident waves, are presented in Fig. 13. The figure illustrates the wave breaking process over a slightly submerged permeable breakwater. The impinging wave forms over the exposed slope of the breakwater a bulk of water with velocities fundamentally tangent to the slope and of high intensity due to flow constriction ($t/T=0.43$). Wave breaking starts just before the seaward edge of the structure crest, with a wave height in breaking of about 1.3 m, and gives rise to a strong onshore-directed jet flow ($t/T=0.6$). The breaking wave propagates over the structure crest, with high vertical velocity components at the toe of the roller being observed ($t/T=0.77$), then partly reforms past the obstacle ($t/T=0.93$). Flow expansion in the deeper waters of the leeside zone goes along with some flow separation occurring at the inner vertex of the breakwater. The velocity field under the transmitted wave is of substantially reduced magnitude compared to the seaward side situation ($t/T=0.93$, $t/T=1$) as a consequence of wave damping at the structure. Within the structure, the flow intensity is considerably lower than in the fluid region, as shown by the very reduced magnitude of the velocity vectors plotted inside the porous media boundaries. As will be more clearly shown hereafter, the highest velocities in the upper part of the breakwater interior are about one order of magnitude lower than the highest velocities reached in the fluid region.

Maximum, mean and minimum velocity profiles at different sections of the structure are displayed in Fig. 14. Upper and lower wave height envelopes and mean water level are also plotted. The considered profiles show details of the aforementioned near-field flow features. The computed maximum horizontal velocities are observed at section 4 right at the onshore end of the breakwater crest, corresponding to the shoreward breaking-induced jet flow, with a magnitude close to 3.5 m/s. One can note that velocities above 2 m/s can be found in every section of the breakwater crest. Maximum vertical velocities also exceed 3 m/s but do not occur at the same location as maximum horizontal velocities. The velocities inside the structure are seen to be negligible compared with the magnitudes reached in the fluid region. Flow in lower regions of the structure solid skeleton is negligibly small compared to external flow given the tested

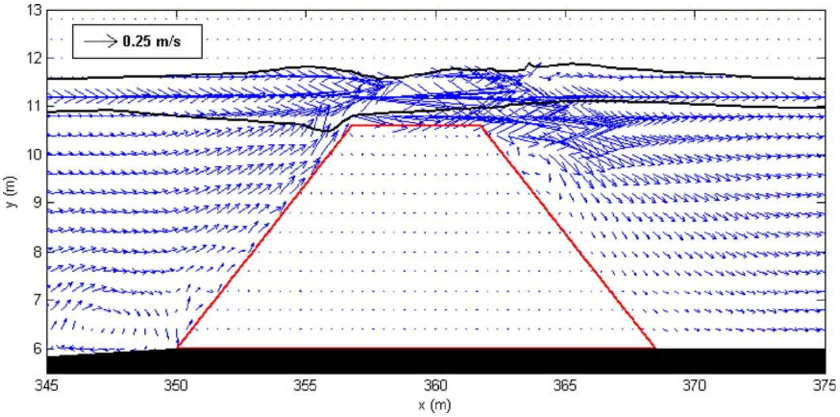

Fig. 16. Mean (time-averaged) velocity field. $F=0.50$ m, $H=1$ m, $T=6$ s, $b=5$ m.

porous material characteristics. The knowledge of the maximum wave-induced velocities at the structure is one of the key inputs for assessment of the effects of the breakwater design features on composition, abundance and distribution of epibiotic assemblages.

The porous flow pattern at the same instants as shown in Fig. 13 is presented in Fig. 15. Vectors scale is enhanced compared to Fig. 13 and velocities in the fluid domain are not included for clarity reasons. Contours of isovalues of the porous Reynolds number are also plotted, drawing a map of the internal flow conditions depending on the location of the breaking wave crest. The pictures reveal how the breaking wave interacts with the first layers of the breakwater, with velocities noticeably decreasing towards the interior of the structure. High Reynolds number conditions ($Re_p > 120\,000$) are achieved near the fluid/porous medium interface as the crest of the breaking wave passes over.

The strong vertical component of the porous flow while the incident wave breaks over the breakwater may deeply influence the structure stability ($t/T=0.43$, $t/T=0.6$), as the rock forming the crest are likely to be removed by the breaking waves and transported to the leeside slope by the inshore jet flow seen in Fig. 13. As the breaking wave reaches the transmission zone ($t/T=0.77$), the slopeward-directed porous flow may work with gravity to move the rock units backslope. Besides, as the tested breakwater is submerged, significant velocities are achieved at the outer edge of the structure crest associated to the backward movement of the waves ($t/T=0.93$), with the subsequent risk of damage. It should be pointed out that rock dislodgement from the structure crest leads to local reductions of the freeboard and consequently increases the stability of the structure.

The time-averaged velocity field in the structure vicinity, displayed in Fig. 16, yields relevant insight on the structure of the near-field flow. The vectorial representations of Figs. 13 and 15 and the profiles shown in Fig. 14 evidence the considerable amount of water transmitted inshore by the breaking waves and the very poor contribution of the porous flow to the process. Mass transport is essentially achieved by overtopping of the breakwater. The figures illustrate the interest of LCS compared to conventional emerged breakwaters regarding inshore waters renovation, which is one of the prime reasons for deployment of this type of structures in recreational areas. From the standpoint of ecological impacts assessment, information on mean flow helps to determine external fertilisation efficiency and serves as input for larvae dispersal models.

References

Burcharth, H.F., Andersen, O.K., 1995. On the one-dimensional steady and unsteady porous flow equations. Coastal Engineering, ELSEVIER 24 (3), 233–257.

Denny, M.W., 1988. Biology and the Mechanics of the Wave-Swept Environment. Princeton University Press, Princeton.

Garcia, N., Lara, J.L., Losada, I.J., 2004. 2-D Numerical analysis of near-field flow at low-crested breakwaters. Coastal Engineering, ELSEVIER 51 (10), 991–1020.

Hirt, C.W., Nichols, B.D., 1981. Computational method for free surface hydrodynamics. Journal of Pressure Vessel Technology, Transactions of the ASME 103 (2), 136–141.

Hsu, T.-J., Sakakiyama, T., Liu, P.L.-F., 2002. A numerical model for wave motions and turbulence flows in front of a composite breakwater. Coastal Engineering, ELSEVIER 46, 25–50.

Kramer, M., Zanuttigh, B., van der Meer J.W., Vidal C., Gironella, F.X., 2005—this volume. 2D and 3D experiments on LCS, Coastal Engineering. ELSEVIER. doi:10.1016/j.coastaleng.2005.09.002.

Lin, P., Liu, P.L.-F., 1998. A numerical study of breaking waves in the surf zone. Journal of Fluid Mechanics 359, 239–264.

Liu, P.L.-F., Lin, P., Chang, K.A., Sakakiyama, T., 1999. Numerical modeling of wave interaction with porous structures. Journal of Waterways, Port, Coastal and Ocean Engineering 125, 322–330.

Liu, P.L.-F., Lin, P., Hsu, T., Chang, K., Losada, I.J., Vidal, C., Sakakiyama, T., 2000. A Reynolds averaged Navier–Stokes equation model for nonlinear water wave and structure interactions. Proceedings of Coastal Structures’00, pp. 169–174.

Losada, I.J., 2003. Modelling the effects of permeable and reflective structures on waves and nearshore flows. In: Lakan, C. (Ed.), Advances in Coastal Modeling, Elsevier Oceanography Series, vol. 67, pp. 189–216.

Loveless, J., Debski, D., MacLeod, A.B., 1998. Sea level set-up behind detached breakwaters. Proceedings of the 26th International Conference on Coastal Engineering, pp. 1665–1678.

Mansard, E.P.D., Funke, E.R., 1980. The measurement of incident and reflected spectra using a least squares method. Proceedings of the 17th International Conference on Coastal Engineering, ASCE, pp. 154–172.

Mayer, S., Madsen, P.A., 2000. Simulation of breaking waves in the surf zone using a Navier–Stokes solver. Proceedings of the 27th International Conference on Coastal Engineering, ASCE 1, 928–941.

Ubbink, O., 1997. Numerical Prediction of two fluid systems with sharp interfaces, PhD Thesis, Mechanical Engineering Dept., Imperical College, University of London, p. 69.

Van Gent, M.R.A., 1994. The modelling of wave action on and in coastal structures. Coastal Engineering, ELSEVIER 22, 311–339.

Vidal, C., Losada, I.J., Martín, F.L., 1998. Stability of near-bed rubble-mound structures. Proceedings of the 26th International Conference of Coastal Engineering, ASCE, pp. 1730–1743.